




# Microstructure and mechanical properties of a laser-based directed energy deposited Mo-Si-Ti alloy

Daniel Schliephake<sup>1,\*</sup> , Sri R. Ramdoss<sup>1</sup>, R. J. Vikram<sup>1</sup>, Gabriely Falcão<sup>1</sup>, Florian Galgon<sup>2</sup>, Hemanth Thota<sup>3</sup>, Frauke Hinrichs<sup>1</sup>, Christopher Zenk<sup>2</sup>, Alexander Kauffmann<sup>1,7</sup>, Yolita Eggeler<sup>3</sup>, Satyam Suwas<sup>4</sup>, Ruth Schwaiger<sup>5,6</sup>, and Martin Heilmaier<sup>1</sup>

<sup>1</sup> Institute for Applied Materials (IAM-WK), Karlsruhe Institute of Technology (KIT), Engelbert-Arnold-Str. 4, 76131 Karlsruhe, Germany

<sup>2</sup> Department of Materials Science and Engineering, Institute II: Materials Science and Engineering for Metals (WTM), Friedrich-Alexander-Universität Erlangen-Nürnberg, 91058 Erlangen, Germany

<sup>3</sup> Microscopy of Nanoscale Structures & Mechanisms (MNM), Laboratory for Electron Microscopy (LEM), Karlsruhe Institute of Technology (KIT), Engesserstr. 7, 76131 Karlsruhe, Germany

<sup>4</sup> Department of Materials Engineering, Indian Institute of Science, Bangalore 560012, India

<sup>5</sup> Institute of Energy and Climate Research (IEK), Forschungszentrum Jülich GmbH, 52425 Jülich, Germany

<sup>6</sup> Chair of Energy Engineering Materials, RWTH Aachen University, 52056 Aachen, Germany

<sup>7</sup> Institute for Materials (IM), Ruhr University Bochum, Bochum, Germany, Universitätsstraße 150, 44801

**Received:** 11 April 2025

**Accepted:** 26 June 2025

© The Author(s), 2025

## ABSTRACT

This study focuses on the linkage between microstructure and mechanical properties at elevated temperatures of a Mo-20Si-52.8Ti (at.%) eutectic alloy produced by directed energy laser deposition (DED-LB). The alloy consists of a body centered cubic solid solution (Mo,Ti,Si)<sub>ss</sub> and a hexagonal (Ti,Mo)<sub>5</sub>Si<sub>3</sub> phase. In addition, a conventional as-cast (AC) alloy with subsequent heat treatment (HT) to further coarsen the microstructure is investigated to rationalize the effect of microstructural length scale on mechanical properties by DED-LB. The fine microstructure produced by DED-LB has a significant effect on the 0.2% offset yield strength at 900 °C compared to AC and HT. This was found to be mainly due to the depletion of Si in (Mo,Ti,Si)<sub>ss</sub> and to the creep contribution caused by the high phase boundary density. By contrast, the effect of interstitial O contamination and texture formation in the (Ti,Mo)<sub>5</sub>Si<sub>3</sub> phase is excluded as a reason of the difference in 0.2% offset yield strength compared to AC and HT.

Handling Editor: Megumi Kawasaki.

Address correspondence to E-mail: daniel.schliephake@kit.edu

<https://doi.org/10.1007/s10853-025-11158-0>

Published online: 08 July 2025

## Introduction

Single crystalline Ni-based superalloys are still the most important materials when it comes to high-temperature structural applications, since they fulfill best the required property portfolio of high strength and creep resistance combined with high temperature oxidation and corrosion resistance [1, 2]. Furthermore, they possess good fatigue resistance and ductility at room temperature [1, 3]. However, the development of new Ni-based superalloys to increase operation temperatures and therefore, the efficiency of e.g. combustion engines, is limited by the solvus temperature of the  $\gamma'$  strengthening phase [4]. Hence, immense continued efforts are ongoing to develop new high-temperature materials such as Mo- and Nb-based silicides [5–7] or refractory high entropy alloys with possibly enhanced temperature capability [8, 9]. Even though all of the aforementioned refractory metal based materials have demonstrated high temperature performance capabilities, none of them fulfil all the property requirements at the same time.

Mo-Si-Ti alloys exhibit the potential to operate at higher temperatures than Ni-based superalloys, since they have comparable strength and creep resistance at even higher temperatures and are also oxidation resistant [10, 11]. In contrast to other Mo-based silicides they also provide pesting resistance, a phenomenon where the formation of volatile  $\text{MoO}_3$  at around 800 °C causes severe material loss and ultimately failure of the alloys by disintegration [12].

The most promising alloy composition in this comparably simple ternary system was identified as Mo-20Si-52.8Ti (all compositions in this article are given in at.%, if not stated otherwise), which forms a eutectic microstructure during casting that is composed of a body-centered cubic  $(\text{Mo,Ti,Si})_{\text{ss}}$  solid solution phase and a hexagonal intermetallic  $(\text{Ti,Mo})_5\text{Si}_3$  phase (note that the order of elements in parentheses represents the content with decreasing quantity from left to right) [10]. This alloy also offers the advantage of lower density compared to Ni-based superalloys and Mo-Si-B alloys (6.2 vs. 8.2–9.6 g/cm<sup>3</sup> [1, 10]), in addition to the high creep and oxidation resistance. Furthermore, the formation of  $(\text{Ti,Mo})_5\text{Si}_3$  precipitates found during recent investigations of the creep behavior promises additional strengthening capability of such alloys [13]. On the downside, the brittle  $(\text{Ti,Mo})_5\text{Si}_3$  phase forms an interconnected network within the Mo-20Si-52.8Ti

alloy and therefore, the brittle-to-ductile transition temperature (BDTT) in three-point-bending is high, around 1100 °C [14]. This is significantly higher than for Mo-Si-B alloys with disconnected intermetallic phases within a continuous Mo solid solution [15, 16]. Recent investigations of off-eutectic Mo-Si-Ti alloy compositions, however, show that the fracture toughness can be increased by reducing the volume fraction of  $(\text{Ti,Mo})_5\text{Si}_3$  [17]. In general, for two-phase microstructures, the deformation behavior relies on the interface mechanics, in particular on the slip transmission across phases depending on their orientation relationships which in turn influences the final deformation texture. The phases  $(\text{Mo,Ti,Si})_{\text{ss}}$  and  $(\text{Ti,Mo})_5\text{Si}_3$  in directionally solidified (DS) Mo-20Si-52.8Ti exhibited a crystallographic OR with  $(123)_{(\text{Mo,Ti,Si})_{\text{ss}}} \parallel (0001)_{(\text{Ti,Mo})_5\text{Si}_3}$  and  $[11\bar{1}]_{(\text{Mo,Ti,Si})_{\text{ss}}} \parallel [11\bar{2}]_{(\text{Ti,Mo})_5\text{Si}_3}$  independent of solidification velocities imposed [18].

Several processing routes have been applied to manufacture silicide-containing Mo-based alloys, Mo-Si-B alloys in particular [15, 19, 20]. Most of these processing techniques, such as arc melting or powder metallurgy (PM) combined with mechanical alloying, are not suited to manufacture complex parts. This is either due to the high BDTT, crack formation during casting or the interstitial contamination, which is detrimental for the ductility [14, 16]. A major challenge for conventional manufacturing processes is the need for extensive mechanical finishing, particularly for complex parts like turbine blades. This is due to the difficulty in machining hard silicide phases.

Additive manufacturing (AM) has been proposed as the solution for producing complex mechanical parts, but a key concern is ensuring crack-free material deposition, since rapid cooling is applied and cyclic heat treatment of the consolidated layers occurs [21, 22]. This may lead to crack formation when the manufacturing temperature is below or cycled around the BDTT. Recently, several attempts were made to process Mo-Si-B and Mo-Si-B-TiC alloys by AM [23–26]. Powder bed fusion by laser (PBF-LB) or electron beam (PBF-EB) require powder of spherical particle shape and in a specific powder size distribution to provide good flowability of the powder [27]. It was shown by Fichtner et al. [23] that it is possible to produce dense and crack-free Mo-16.5Si-7.5B by PBF-LB using pre-heating

temperatures of 1200 °C. In addition to that, subjecting the powder to heat treatment in an Ar atmosphere is required as this minimizes O and N contamination as well as moisture which are critical to crack formation. The same pre-heating temperature was necessary during the processing of Mo-5Si-10B-10TiC (at.%) by PBF-EB [26]. In comparison to a Mo-8.9Si-7.7B alloy manufactured using PM processing of gas atomized powder, PBF-LB processing of Mo-16.5Si-7.5B demonstrates a reduction of the BDTT by approximately 100 °C to approx. 1000 °C [23]. Both alloys possess a matrix consisting of intermetallic phases and the reduction of the BDTT is attributed to the formation of dendritic Mo solid solution breaking up the matrix character of the intermetallic phases by the PBF-LB processing. However, PBF-LB results in ultrafine grain and phase sizes, and hence, in a reduced creep resistance compared to ingot metallurgical materials [23]. It was also shown recently, that laser metal deposition (LMD) can be used to manufacture dense and crack-free Mo-13Si-7.5B alloy [24]. The microstructure of LMD processed Mo-Si-B is much finer compared to the same alloy manufactured by casting and the intermetallic phases are embedded within the solid solution matrix. The mechanical behavior of this material was only determined by microhardness measurements and both processing conditions, casting and LMD, yielded similar hardness of around 16 GPa [24].

It is well established, that AM can lead to the formation of textured parts, due to the directional solidification front and the temperature gradient along the build direction [28], but no further information on texture formation during LMD or PBF-LB of Mo-Si-B alloys have yet been provided in literature. However, the formation of a crystallographic texture is possible in Mo-20Si-52.8Ti when processed by AM, as previously demonstrated for the DS process [18].

Therefore, this study aims to identify the relationship between AM and resulting microstructure using laser-based directed energy deposition (DED-LB), a process similar to LMD. Furthermore, we aim at understanding how DED-LB influences the yield strength between room temperature and 1100 °C along and perpendicular to the build direction in comparison to ingot metallurgical material. To include the different microstructural length scales due to the different processes a batch of the cast alloy was also investigated before and after an annealing process. This approach was chosen in order to compare the

mechanical properties within the same alloying system, rather than comparing them with Mo-Si-B and Mo-Si-B-TiC alloys. The latter have a different microstructure to Mo-Si-Ti and have mainly been investigated in terms of hardness [23, 24, 26] and four-point bending [25]. Notably, DED-LB was chosen over PBF-LB/EB due to the unavailability of a PBF-LB system with preheating capabilities of up to 1200 °C as used in Ref. [23], and the occurrence of intense smoke events during PBF-EB experiments, which made processing parts impossible.

## Materials and experimental methodology

Mo-20Si-52.8Ti (in at.%) powder was produced by Electrode Induction Gas Atomization (EIGA) by GfE Metalle und Materialien GmbH (Nürnberg, Germany). Powder particles with sizes ranging from 53 µm to 100 µm were sieved from the as-received powder batch. Details on the powder processing of Mo-20Si-52.8Ti can be found in Ref. [29]. For comparison Mo-20Si-52.8Ti was synthesized from bulk elemental Mo (99.8% purity), Ti (99.95%) and Si (99.99%) by arc melting in an Ar atmosphere. An AM0.5 arc melter (Edmund Bühler GmbH, Bodelshausen, Germany) was used equipped with a water-cooled Cu crucible. A detailed description of the process can be found in Ref. [10]. One part of the alloy batch was subsequently heat treated at 1600 °C for 150 h in Ar to significantly coarsen the microstructure.

DED-LB was performed using an InssTek (Daejeon, South Korea) MX600 enclosed in an MBraun (Munich, Germany) Argon chamber. The laser source was a 1070 nm Yt:YAG fiber laser from IPG Photonics (Marlborough, USA) with a spot diameter of 500 µm in the working plane. The scan pattern used was a cross-snake pattern with 400 µm line offset spanning 11 × 11 mm and the deposition head was moved with 20 mm/s. A small – 15 × 15 × 10 mm Ti64 substrate was thermally isolated from the machine table by a graphite felt and 10 layers (200 µm nominal layer height) of Ti64 powder (in wt.% by TEKNA (Sherbrooke, Canada) with particle size of 45–100 µm) were deposited with – 0.7 g/min feed rate and 360 W laser power in order to improve bonding with the substrate material and to reach high processing temperatures. Afterwards, the powder source was switched to – 1.5 g/min Mo-20Si-52.8Ti powder

deposited with a laser power of 300–340 W, all other parameters kept constant.

Throughout the manuscript DED will refer to Mo-Si-Ti manufactured by the DED-LB process with *v* (vertical) and *h* (horizontal) indicating the orientation of which the samples were taken parallel and perpendicular to the build direction (BD), respectively. The as-cast condition will be abbreviated by AC and the coarsened condition of AC is designated HT in what follows.

Microstructural analysis by scanning electron microscopy (SEM) was conducted on samples prepared by grinding using SiC paper up to grit P4000. Subsequent to grinding, polishing was performed with 3 and 1  $\mu\text{m}$  diamond suspension before final polishing with a colloidal silica suspension. A LEO 1530 Zeiss FEG (Carl Zeiss AG, Oberkochen, Deutschland) SEM operated at 20 kV acceleration voltage was used in secondary electron (SEM-SE) and backscattered electron (SEM-BSE) contrast. For energy-dispersive X-ray spectroscopy (SEM-EDX), an EVO 50 Zeiss SEM (Carl Zeiss AG, Oberkochen, Deutschland) was used. Electron backscatter diffraction (SEM-EBSD) was performed in a Zeiss Auriga 60 SEM equipped with an EDAX DigiView EBSD camera (Ametek, Berwyn, Pennsylvania, USA). An acceleration voltage of 20 kV was used to scan a hexagonal grid of an area of  $(80 \times 80) \mu\text{m}^2$  with a step size of 0.2  $\mu\text{m}$ . SEM-BSE micrographs of the powder were taken with particles placed on a carbon tape to analyze the particle size distribution and aspect ratio of the particles with ImageJ [30]. Scanning transmission electron microscopy (STEM) on an FEI Tecnai Osiris at 200 kV equipped with a quad silicon drift detector setup (Super-X) was performed for STEM-EDX analysis. Furthermore, ImageJ was used to determine porosity, volume fraction of phases and phase boundary density using the SEM-BSE micrographs of the bulk material.

The phase boundary density was determined by applying a linear intersection approach [31] using:

$$P = 2 \frac{\bar{N}}{L} \quad (1)$$

Thereby,  $\bar{N}$  is the number of intersections and  $L$  the total length of the sections.

To investigate the mechanical behavior, compression test specimens of  $(3 \times 3 \times 5) \text{ mm}^3$  in dimensions were prepared by electrical discharge machining. Compression tests with an initial strain rate

of  $10^{-3} \text{ s}^{-1}$  with respect to the sample height were performed using a Z100 universal testing device by Zwick (ZwickRoell, Ulm, Germany) equipped with a Maytec vacuum furnace (Maytec Mess- und Regeltechnik GmbH, Singen, Germany) at temperatures ranging from 900 to 1100 °C. Additional compression tests were carried out at 900 °C with initial strain rates of  $10^{-4} \text{ s}^{-1}$  and  $10^{-5} \text{ s}^{-1}$ , to study the strain rate dependence of stress at elevated temperatures.

Compression creep tests were performed at 900 °C with a constant true stress of 200 MPa. Load and displacement were monitored during the compression and compression creep tests and were converted during the data acquisition into true strain and true stress assuming constant sample volume during deformation. Vickers hardness was measured on polished surfaces using a QNess Q10+ (ATM Qness GmbH, Mammeln, Germany) microhardness tester at a load of 0.98 kg (HV1).

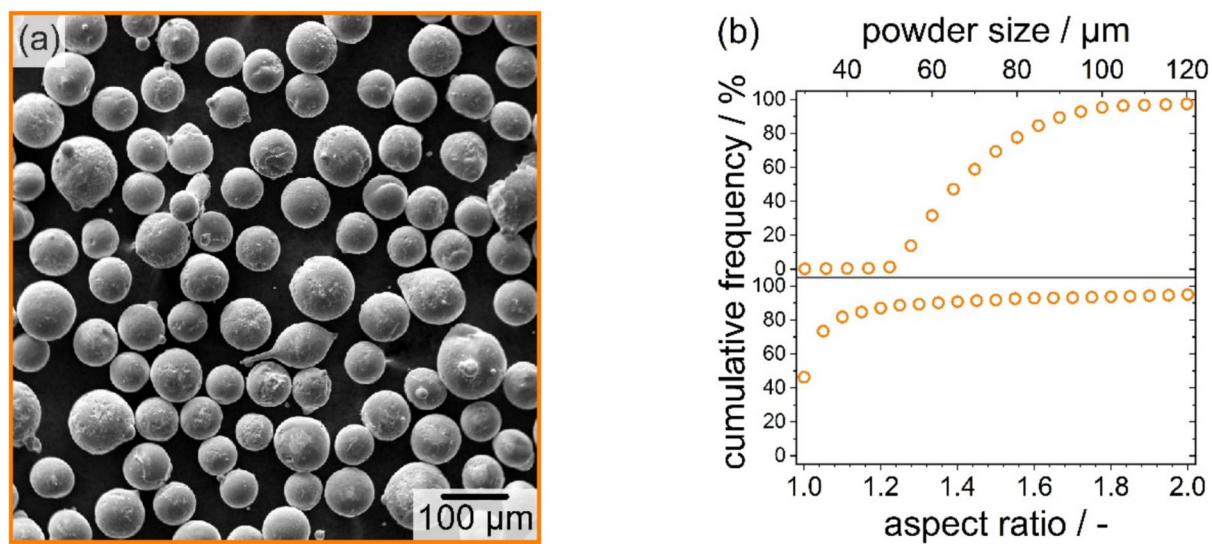
X-ray diffraction (XRD) was performed using a D2 Phaser (Bruker Corp., Billerica, MA, USA) equipped with a LynexEye line detector in Bragg-Bretano geometry on polished surfaces in  $0.01^\circ$  steps with a Cu X-ray tube operated at 30 kV and 10 mA. The incident radiation was filtered by means of a Ni foil. The lattice parameters were determined by extrapolating the peak positions using a modified Nelson–Riley approach [32].

## Results

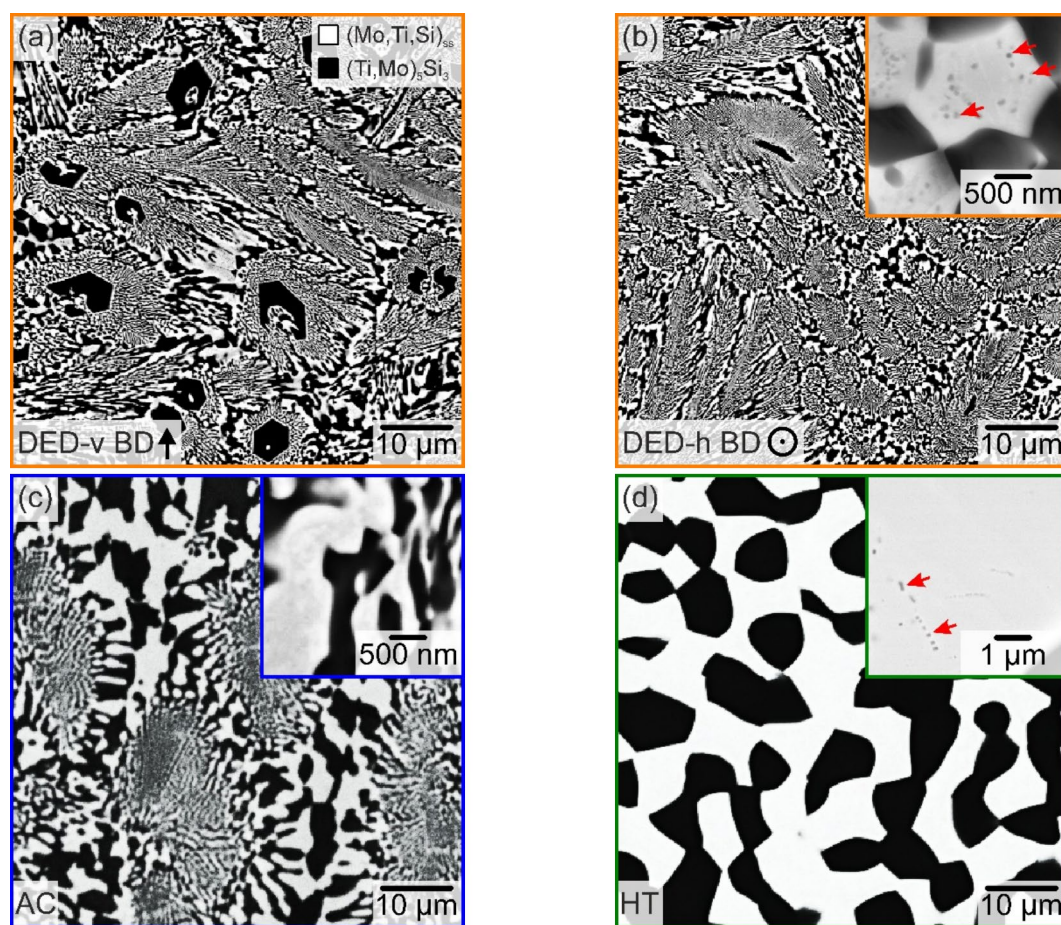
The initial microstructures of the three processed conditions were examined using SEM. Figure 1a illustrates the morphology of the initial powder, comprising spherical particles with partial satellite decoration. Figure 1b displays the particle size distribution and sphericity of the powder particles after sieving with -100 and -53  $\mu\text{m}$  mesh sizes. It is evident from Fig. 1b that 90% of the volume fraction of the particles fall within the range of 50 to 90  $\mu\text{m}$ , with  $D_{90}$  at 90  $\mu\text{m}$  and 90% of the particles possessing an aspect ratio of less than 1.4. This range is deemed sufficient to ensure favorable flowability and packing during the manufacturing process. The O contamination of the powder was reported in Ref. [29] as  $(1740 \pm 60) \text{ wt.}\text{-ppm}$ .

Figure 2 displays the microstructures of Mo-20Si-52.8Ti manufactured by DED-LB as well as in the AC and HT conditions. The microstructures of all





**Figure 1** Mo-20Si-52.8Ti powder sieved between -100 and -53 mesh size showing **a** SEM-SE micrograph and **b** particle size distribution and sphericity



**Figure 2** microstructure **a** DED-v, **b** DED-h, **c** AC and **d** HT. Red arrows in the inserted details indicate  $(\text{Ti,Mo})_5\text{Si}_3$  precipitates in  $(\text{Mo,Ti,Si})_{ss}$

**Table 1** Summarized information on volume fraction of phases, phase boundary density and lattice parameter for (Mo,Ti,Si)<sub>ss</sub>. Data for AC and HT were taken from Ref. [33]

|     | Vol. fraction<br>(Ti,Mo) <sub>5</sub> Si <sub>3</sub> / % | Phase boundary<br>density / $\mu\text{m}^{-1}$ | Lattice param-<br>eter (Mo,Ti,Si) <sub>ss</sub> /<br>nm |
|-----|---|--|---|
| DED | 50 ± 2  | 3.1 ± 0.4                                      | 0.3173 ± 0.0003   |
| AC  | 53 ± 2  | 0.6 ± 0.02                                     | 0.3167 ± 0.0007   |
| HT  | 50 ± 2  | 0.2 ± 0.04                                     | 0.3164 ± 0.0005   |

conditions consist of (Mo,Ti,Si)<sub>ss</sub> and (Ti,Mo)<sub>5</sub>Si<sub>3</sub> as confirmed by XRD [10]. No cracks were observed for the DED condition and the porosity was determined by image analysis to be less than 1 vol%. Microstructural parameters such as volume fraction of (Ti,Mo)<sub>5</sub>Si<sub>3</sub>, phase boundary density and lattice parameter of (Mo,Ti,Si)<sub>ss</sub> are summarized in Tab. 1. The volume fraction of phases is the same for all processing conditions. The phase boundary density is (0.6 ± 0.02)  $\mu\text{m}^{-1}$  for AC and decreases during heat treatment to (0.2 ± 0.04)  $\mu\text{m}^{-1}$  for HT, while it is (3.1 ± 0.4)  $\mu\text{m}^{-1}$  for DED. At the same time the lattice parameter of (Mo,Ti,Si)<sub>ss</sub>, as determined by XRD and refined by Nelson–Riley approach is highest for DED, while it is comparable for AC and HT.

Within the (Mo,Ti,Si)<sub>ss</sub>, (Ti,Mo)<sub>5</sub>Si<sub>3</sub> precipitates identified using SEM–EDX were found, as displayed in the insert in Fig. 2b. This is consistent with recent investigations on the creep behavior of Mo–20Si–52.8Ti in AC condition which confirmed the formation of (Ti,Mo)<sub>5</sub>Si<sub>3</sub> precipitates in (Mo,Ti,Si)<sub>ss</sub> already after casting by transmission electron microscopy [13]. However, the number of precipitates appears lower compared to the precipitates observed in DED condition, as can be seen from the inserts in Fig. 2b–d. In the HT condition the number of (Ti,Mo)<sub>5</sub>Si<sub>3</sub> precipitates is still small compared to the DED condition and the precipitates are mainly be straight aligned within (Mo,Ti,Si)<sub>ss</sub>. This has already been reported for the AC condition in Ref. [13] and is associated with dislocation arrays acting as nucleation sites for the precipitation reaction. During the DED processing, the remelting of the previously deposited layer happens concurrent to the deposition of the new layer, which enables sufficient diffusion of Si to form precipitates. This leads to a depletion of Si in (Mo,Ti,Si)<sub>ss</sub>, as confirmed by STEM-EDX analysis. The dissolved Si content is (0.8 ± 0.1) at.% Si in (Mo,Ti,Si)<sub>ss</sub> for the DED

condition as compared to (2.4 ± 0.3) at.% Si in AC [33]. The  $d_{50}$  and  $d_{90}$  of the particles is 75–125 nm, respectively. Finally, no precipitates of (Mo,Ti,Si)<sub>ss</sub> within (Ti,Mo)<sub>5</sub>Si<sub>3</sub> were identified within the resolution limits of SEM-BSE. No (Ti,Mo)<sub>5</sub>Si<sub>3</sub> precipitates were found in the HT condition.

Tab. 2 summarizes the results of SEM–EDX for all three conditions showing that the composition is the same irrespective of the processing route.

SEM-EBSD was performed for DED-h and inverse pole figure (IPF) maps are shown in Fig. 3a, b for (Mo,Ti,Si)<sub>ss</sub> and (Ti,Mo)<sub>5</sub>Si<sub>3</sub>, respectively. No preferred orientation of (Mo,Ti,Si)<sub>ss</sub> is observed, while (Ti,Mo)<sub>5</sub>Si<sub>3</sub> exhibits a fiber texture with the (0001) direction parallel to the build direction of the DED sample. This is quantified by the orientation distribution in multiples of uniform distribution (m.u.d.) in the IPF. While (Mo,Ti,Si)<sub>ss</sub> possesses a maximum of 1.5 m.u.d. between (001) and (111), (Ti,Mo)<sub>5</sub>Si<sub>3</sub> has its maximum of 4.2 m.u.d. in the (0001) direction. Pole figure analysis at two interfaces was done to match the pole locations of each phase in the same reference frame to understand the OR (for simplicity the analysis is shown for interface 1 only). It was identified that the (123) plane of (Mo,Ti,Si)<sub>ss</sub> is parallel to the basal plane (0001) of (Ti,Mo)<sub>5</sub>Si<sub>3</sub>, and the [111] direction of (Mo,Ti,Si)<sub>ss</sub> is parallel to the [11 $\bar{2}$ 0] of (Ti,Mo)<sub>5</sub>Si<sub>3</sub> with minor deviation about the c-axis indicating a crystallographic OR existing between the phases of (123)<sub>(Mo,Ti,Si)<sub>ss</sub></sub> || (0001)<sub>(Ti,Mo)<sub>5</sub>Si<sub>3</sub></sub> and [11 $\bar{1}$ ]<sub>(Mo,Ti,Si)<sub>ss</sub></sub> || [11 $\bar{2}$ 0]<sub>(Ti,Mo)<sub>5</sub>Si<sub>3</sub></sub>. A similar OR was observed by Vikram et. al [18] for DS of Mo–20Si–52.8Ti.

Vickers hardness was determined as (639 ± 20) HV1, (677 ± 60) HV1 and (704 ± 62) HV1 for the HT, AC and DED-v conditions, respectively. The hardness of AC after conducting creep experiments at 100 MPa and at 1200 °C for different conditions, e.g. at the minimum creep rate and after 10% plastic strain, was determined to evaluate the effect of the particle size of (Ti,Mo)<sub>5</sub>Si<sub>3</sub> precipitates within (Mo,Ti,Si)<sub>ss</sub>. Vickers hardness of (682 ± 15) HV1 and (670 ± 26) HV1 were determined after reaching the minimum creep rate and 10%

**Table 2** Summary of SEM–EDX results for all three conditions

| Condition | Mo / at.%  | Si / at.%  | Ti / at.%  |
|-----------|------------|------------|------------|
| AC        | 26.0 ± 0.4 | 20.6 ± 0.1 | 53.4 ± 0.4 |
| HT        | 25.0 ± 0.1 | 21.4 ± 0.2 | 53.6 ± 0.1 |
| DED       | 26.8 ± 0.1 | 19.9 ± 0.2 | 53.2 ± 0.2 |



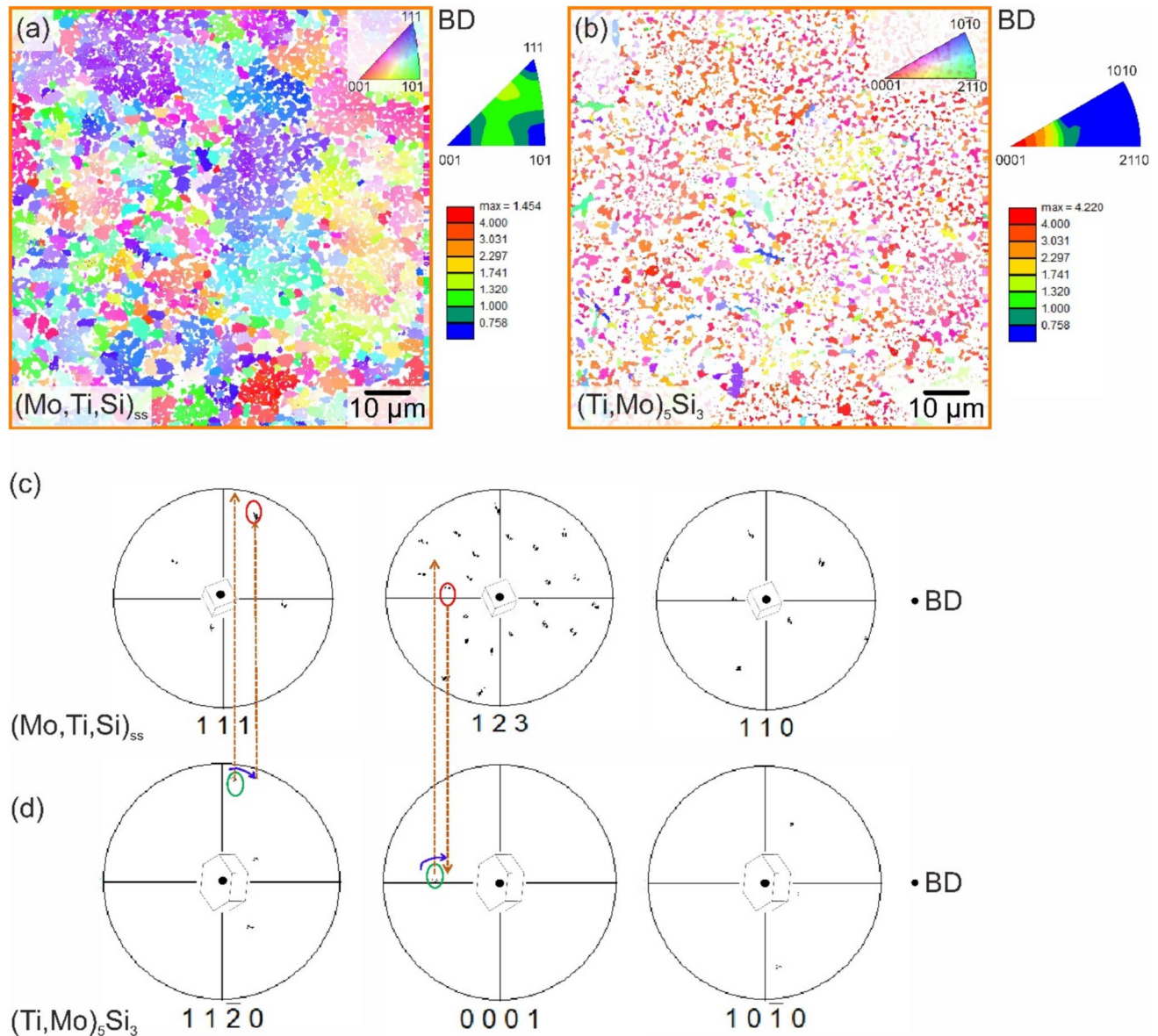


**Figure 3** Orientation imaging microscopy analysis of DED-h with the build direction out of plane showing **a** and **b** the color-coded IPF map of the  $(\text{Mo,Ti,Si})_{\text{ss}}$  and  $(\text{Ti,Mo})_5\text{Si}_3$ , respectively.

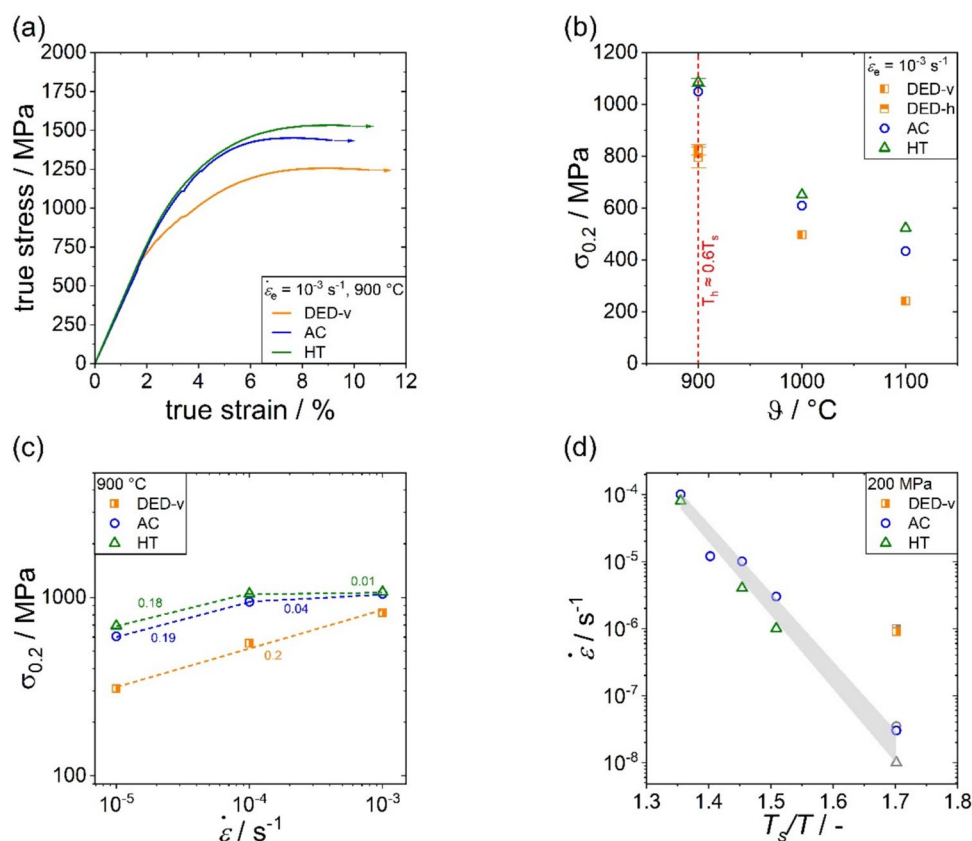
The orientation distribution in m.u.d. of each phase is shown next to the IPF map. In **c** and **d** the OR between  $(\text{Mo,Ti,Si})_{\text{ss}}$  and  $(\text{Ti,Mo})_5\text{Si}_3$  is visualized

plastic strain (corresponding to 0.5–2.5 h at 1200 °C, respectively). Figure 4a shows representative true stress–strain ( $\sigma_t - \epsilon_t$ ) data of DED-v, AC and HT tested in compression at 900 °C. AC and HT have the highest maximum strength compared to DED-v. DED-h is not shown here due to a nearly identical stress–strain curve compared to DED-v. 0.2% offset yield strength at 900 °C of DED-v and DED-h is the same and, thus, independent of the compression direction relative

to the build direction. No tests were performed for DED-h at higher temperatures.

The temperature dependent 0.2% offset yield strength  $\sigma_{0.2}$  is shown in Fig. 4b. For all tested temperatures, the HT and AC conditions possess higher  $\sigma_{0.2}$  compared to DED-v. At 900 °C  $\sigma_{0.2}$  of AC and HT are similar, while HT consistently shows a slightly higher  $\sigma_{0.2}$  with increasing testing temperature. The homologous temperature  $T_h$  at 900 °C is around 0.6 (according to the solidus temperature  $T_s$  of 1723 °C,

**Figure 4** Mechanical behavior determined by compression tests for DED, AC and HT showing **a** representative curves of true stress vs. true strain diagram at 900 °C and  $10^{-3} \text{ s}^{-1}$ , **b** the temperature dependent  $\sigma_{0.2}$  (dashed vertical line indicates  $T_h$  of approx. 0.6), **c** the strain rate dependent  $\sigma_{0.2}$  at 900 °C and **d** the Arrhenius plot for compressive creep at 200 MPa (grey data points are extrapolated from **c** to 200 MPa)



calculated in Ref. [10]) and is marked with a discontinuous vertical red line in Fig. 4b. It is worth noting here, that all three conditions fail without any plastic deformation within the elastic regime when tested at 800 °C. Therefore, no results regarding  $\sigma_{0.2}$  are shown here for tests conducted below 900 °C.

Figure 4c displays  $\sigma_{0.2}$  for different initial strain rate  $\dot{\epsilon}$  for AC, HT and DED-v at 900 °C in a double logarithmic diagram.  $\sigma_{0.2}$  for DED-v increases with higher strain rates. AC and HT show similar behavior with an increase of  $\sigma_{0.2}$  between  $10$  and  $10^{-4} \text{ s}^{-1}$ , while  $\sigma_{0.2}$  remains constant between  $10$  and  $10^{-3} \text{ s}^{-1}$ . The slope  $m$  for  $\sigma_{0.2}$  vs.  $\dot{\epsilon}$  in Fig. 4c for DED-v is 0.2 and for AC and HT 0.19 and 0.18, respectively, for  $\dot{\epsilon} < 10^{-4} \text{ s}^{-1}$ . When the strain rate increases to  $10^{-3} \text{ s}^{-1}$ , the slope changes to 0.01 and 0.04, respectively, for AC and HT. The slope can be interpreted as strain rate sensitivity  $m$  at a certain true strain, in this case at 0.2%. The strain rate sensitivity can be calculated as:

$$m = \frac{\partial \ln(\sigma)}{\partial \ln(\dot{\epsilon})} \quad (2)$$

where,  $\sigma$  is the stress and  $\dot{\epsilon}$  is the strain rate. Strain rate sensitivity can also be expressed as:

$$m = \frac{1}{n} \quad (3)$$

where  $n$  is the apparent stress exponent for creep in metals and alloys [34]. Therefore, the stress exponent can be calculated as:

$$n = \frac{1}{m} \quad (4)$$

from Eq. (3). For DED,  $n$  is 5 for the full range of strain rates tested at 900 °C, while for AC and HT,  $n$  is  $-25$  for strain rates below  $10^{-4} \text{ s}^{-1}$  and  $-5$  above  $10^{-4} \text{ s}^{-1}$ .

Figure 4d displays the creep data of AC and HT from previous investigations using the Arrhenius plot with a temperature dependence normalized by  $T_s$  [10, 11, 13]. In addition, the results shown in Fig. 4c were extrapolated towards  $\sigma_{0.2}$  of 200 MPa using the slopes determined from the compression tests at different  $\dot{\epsilon}$ . The data points by the extrapolation are visualized by the grey data points in Fig. 4d, while the data obtained from compression creep tests at 200 MPa true stress



are highlighted in the respective color. It can be seen, that the extrapolated  $\dot{\epsilon}$  at 900 °C for AC and HT fits well with the  $\dot{\epsilon}$  estimated from compression creep tests (highlighted by the grey area), while  $\dot{\epsilon}$  for DED-v is significantly higher. In order to confirm the extrapolation, a compression creep test for DED-v and AC was performed at 900 °C and 200 MPa true stress with the minimum creep rate matching well with the  $\dot{\epsilon}$  by the extrapolation from Fig. 4c.

The microstructure of DED-v after compression testing at 900 °C is displayed in Fig. 5. The compression test was deliberately stopped at approx. 6% true plastic strain. It can be seen, that cracks parallel to the loading direction (LD) in  $(\text{Ti},\text{Mo})_5\text{Si}_3$  appeared in the post mortem microstructure, while no cracks were observed in  $(\text{Mo},\text{Ti},\text{Si})_{\text{ss}}$ . In addition, no coarsening of the  $(\text{Ti},\text{Mo})_5\text{Si}_3$  precipitates was observed after the compression tests.

## Discussion

As it was previously reported for Mo-Si-B and other refractory alloys [23, 24], the DED process can also be used to manufacture crack-free and dense specimens of a eutectic Mo-20Si-52.8Ti alloy. The volume fraction of pores in the DED condition with less than 1 vol.% in this work is lower compared to the 2.1 vol.%

determined for Mo-13Si-7.5B manufactured by LMD [24] even though  $D_{90}$  is twice as large for the powder used here. Previous investigations on the effect of powder size distribution indicate that smaller powder sizes will result in less porosity [35]. Nevertheless, the high sphericity of the powder and the lower  $T_s$  (1723 °C) of Mo-20Si-52.8Ti compared to Mo-13.5Si-7.5B (–2000 °C) seem to support the solidification behavior and to reduce porosity.

The finer microstructure and higher phase boundary density of the DED condition compared to AC are a result of a higher solidification rate during the DED process than in the casting process [36–38]. The cooling rate in the DED process varies from  $10^3$  to  $10^5 \text{ K s}^{-1}$  [39, 40] and is rapid during the initial stages resulting in non-equilibrium conditions. Consequently, the size of the eutectic colonies in the initially cooled region is finer, as evidenced by the variation in phase boundary distances between different eutectic colonies in the microstructure. This is also depicted in Fig. 2c, where the spacing of lamellae between inter- and intra-colony regions differs. The increased cooling rate results in an increase of the curvature of the dendrite tips which subsequently yields an increase of the driving force for heterogeneous nucleation resulting in finer regions [41].

At RT, the hardness of DED is by tendency higher compared to AC and HT, which can be expected due to the much higher phase boundary density in DED. Similar results have been reported earlier also for Mo-9Si-8B manufactured by a conventional PM route using mechanical alloying, cold and hot isostatic pressing compared to consolidated Mo-9Si-8B using the field assisted sintering technique (FAST) [16]. FAST results in a much finer microstructure and a higher hardness of 862 HV1 compared to 604 HV1. The effect of  $(\text{Ti},\text{Mo})_5\text{Si}_3$  precipitates on the RT hardness is insignificant. This can be seen by determining the hardness of AC after reaching different stages of creep at 100 MPa and at 1200 °C, which also means different exposure times and ultimately different particle sizes for  $(\text{Ti},\text{Mo})_5\text{Si}_3$  according to Thota et al. [13]. For AC with almost no precipitates the hardness is  $(677 \pm 60) \text{ HV1}$ , while it is  $(682 \pm 15) \text{ HV1}$  after reaching the minimum creep rate (0.5 h at 1200 °C) and  $(670 \pm 26) \text{ HV1}$  after 10% of plastic strain (2.5 h at 1200 °C). The size of the precipitates changes between the later three stages from 78 to 145 to 190 nm ( $D_{90}$ ) [13]. The  $D_{90}$  in DED is 125 nm, which is larger than the size of the  $(\text{Ti},\text{Mo})_5\text{Si}_3$  precipitates in the AC condition. Therefore, a similar

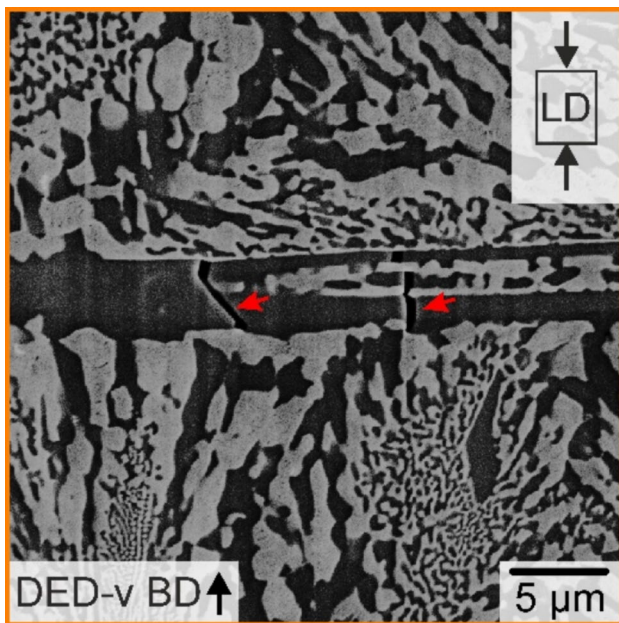


**Figure 5** SEM-BSE micrograph of DED-v after compression test at 900 °C with approx. 6% true plastic strain

contribution to the hardness is to be expected from the  $(\text{Ti},\text{Mo})_5\text{Si}_3$  precipitates. The opposite is expected for the solid solution strengthening by Si, which is considered to be a potent solid solution strengthening element [20], but consumed in the  $(\text{Ti},\text{Mo})_5\text{Si}_3$  precipitates. The opposing trends of the two strengthening mechanisms will be discussed in more detail later in the manuscript. With  $(2.4 \pm 0.3)$  at.% Si dissolved in  $(\text{Mo},\text{Ti},\text{Si})_{\text{ss}}$  in AC [34] compared to only  $(0.8 \pm 0.1)$  at.% Si in  $(\text{Mo},\text{Ti},\text{Si})_{\text{ss}}$  in DED, a higher hardness would be expected for AC. As this is not the case, the phase boundary density, which causes a much finer microstructure in DED, is expected to overcompensate the higher hardness in DED compared to AC and HT.

However, at higher temperatures the  $\sigma_{0.2}$  of the DED condition is smaller than of AC and HT. This can be rationalized based on (i) the O concentration in the alloy, (ii) the texture in  $(\text{Ti},\text{Mo})_5\text{Si}_3$ , (iii) the influence of  $(\text{Ti},\text{Mo})_5\text{Si}_3$  formation on the strengthening of the  $(\text{Mo},\text{Ti},\text{Si})_{\text{ss}}$  phase, and (iv) the contribution of creep deformation to the onset of plastic deformation due to high phase boundary density and a  $T_h$  of almost 0.6 for this alloy composition [13]. It is difficult to conduct a more detailed and quantitative analysis of the difference in yield strength and the respective influence of the microstructural length scale using the Hall–Petch relationship, as the testing temperatures are close to  $T_h = 0.6T_s$  or above, and therefore invalid. Additionally, the contribution of the silicide phase to plastic deformation is negligible (see Fig. 5).

First, the O content of the DED condition is supposed to be much higher compared to AC and HT. According to Ref. [29] the powder used for DED contains up to  $(1760 \pm 60)$  wt.-ppm O, while O concentration in arc melted Mo-Si-Ti alloys was previously reported to be 49 wt.-ppm [14]. A higher O concentration will lead to O segregation towards grain and phase boundaries due to the limited solubility in Mo and ultimately lead to decrease in grain boundary cohesion [42]. Excess O could also lead to the formation of  $\text{SiO}_2$  particles within the grains or along grain boundaries, as previously observed in Mo-Si-B alloys manufactured by PM [16]. This will not only lead to brittle behavior, but also reduce the alloys strength. However, the solubility of oxygen in the  $(\text{Ti},\text{Mo})_5\text{Si}_3$  phase is expected to be much higher, as it is reported for stoichiometric  $\text{Ti}_5\text{Si}_3$  with up to 11 at.% [43]. This will prevent O segregation and its influence on brittle behavior and decrease in macroscopic strength due to brittle failure of the alloy along phase boundaries

before reaching  $\sigma_{0.2}$ . Assuming that all O will be dissolved in  $(\text{Ti},\text{Mo})_5\text{Si}_3$  would result in a maximum O solubility of around 5 at.%, given that the vol. fraction of the silicide phase is approx. 50%. This is in agreement with (i) earlier investigations by Tirunilai et al. [14] of eutectic Mo-20Si-52.8Ti where no influence of the O content has been observed regarding the BDTT, (ii) also with observations that embrittlement of Mo can still occur even when the O concentration drops below 100 ppm [44] and (iii) that no  $\text{SiO}_2$  particles were observed during TEM investigations within  $(\text{Mo},\text{Ti},\text{Si})_{\text{ss}}$  and  $(\text{Ti},\text{Mo})_5\text{Si}_3$  or along phase boundaries, neither in the current investigation nor in Refs. [13, 34]. Furthermore, an increased O content will also contribute to solid solution strengthening, which was not observed here. Therefore, it can be concluded, that the higher oxygen concentration in the DED condition is not the reason for the lower  $\sigma_{0.2}$ .

Second, the  $\langle 0001 \rangle$  fiber texture along the build direction observed in  $(\text{Ti},\text{Mo})_5\text{Si}_3$  can influence the mechanical behavior of the DED alloy. Investigations on the plastic deformation of single crystals of  $\text{Ti}_5\text{Si}_3$  have shown, that single crystals loaded in  $\langle 0001 \rangle$  do not plastically deform below 1400 °C [45]. Furthermore, the stress required to induce plastic strain at 1400 °C is around 1200 MPa and, therefore, far higher than the  $\sigma_{0.2}$  of the DED condition of approx. 800 MPa at 900 °C. This also leads to the conclusion, that  $(\text{Ti},\text{Mo})_5\text{Si}_3$  will not contribute to the plastic strain observed for all conditions even though the  $(\text{Ti},\text{Mo})_5\text{Si}_3$  phase exists as a continuous network in the microstructure. This is experimentally confirmed by the cracks observed in  $(\text{Ti},\text{Mo})_5\text{Si}_3$  subsequent to compression tests at 900 °C (see Fig. 5). These cracks are aligned parallel to the loading direction due to the deformation of the more ductile  $(\text{Mo},\text{Ti},\text{Si})_{\text{ss}}$  phase. Therefore, the texture formation during DED can be excluded as a reason for the lower  $\sigma_{0.2}$  compared to AC and HT.

Third, the observed formation of a high number of  $(\text{Ti},\text{Mo})_5\text{Si}_3$  precipitates (see Fig. 2b) can potentially lead to a strengthening contribution, as it is seen for  $\text{Ti}_5\text{Si}_3$  reinforced Ti alloys for example [46]. However, the formation of  $(\text{Ti},\text{Mo})_5\text{Si}_3$  precipitates will deplete Si in  $(\text{Mo},\text{Ti},\text{Si})_{\text{ss}}$  and therefore reduce the contribution by solid solution strengthening. Compared to the AC with  $(2.4 \pm 0.3)$  at.% Si in  $(\text{Mo},\text{Ti},\text{Si})_{\text{ss}}$  [34], only  $0.8 \pm 0.1$  at.% Si in  $(\text{Mo},\text{Ti},\text{Si})_{\text{ss}}$  was observed in DED. The Si content in  $(\text{Mo},\text{Ti},\text{Si})_{\text{ss}}$  of the DED condition indicates, that the processing temperature during DED was around 1100 °C, as this corresponds to

the maximum solubility of Si in Mo [47]. Si is known to be the most potent solid solution strengthener in Mo alloys [44]. The formation of a higher number of coarse  $(\text{Ti},\text{Mo})_5\text{Si}_3$  precipitates compared to the AC and HT condition could, therefore, lead to an overall decrease in strength of the material at higher temperatures. The reduction in silicon content within the DED process is partly evident in the XRD results, showcasing a higher lattice parameter compared to those of AC and HT. This increase in lattice constant is the result of the reduced silicon content within the solid solution, as shown in this work and stated by Krüger et al. [48]. At the same time, the reduced Ti content in  $(\text{Mo},\text{Ti},\text{Si})_{\text{ss}}$  will result in a slight decrease of the lattice constant according to Ref. [49]. The analysis of each strengthening contribution is complex and further investigations regarding compositional changes in the  $(\text{Mo},\text{Ti},\text{Si})_{\text{ss}}$  phase during the  $(\text{Ti},\text{Mo})_5\text{Si}_3$  formation are difficult to observe statistically relevant in such fine microstructures. Nevertheless, recent investigations on the creep behavior of the AC condition [13] show that this can lead to a depletion in Si to 1.3 at.%. Sturm et al. [50] have investigated the effect of Si on the mechanical behavior of PM manufactured Mo-Si alloys. The  $\sigma_{0.2}$  at 816 °C for Mo-0.34Si and Mo-1.69Si, which have a difference in Si concentration of 1.35 at.% Si, were determined to be 150 MPa and 331 MPa. A similar observation was made by Jain and Kumar who studied a Mo-3Si-1.3B solid solution alloy [20]. The Si content varied in two regions of the extruded alloy, allowing the authors to investigate the influence of Si on the yield strength at 1200 °C. The solid solution alloy with – 1 at.% Si in  $(\text{Mo},\text{Si})_{\text{ss}}$  had a yield strength of 110 MPa, whereas the alloy with – 2 at.% Si in  $(\text{Mo},\text{Si})_{\text{ss}}$  possess a yield strength of 220 MPa. Therefore, a similar effect can be expected here for the DED compared to AC and HT tested at 900 °C.

Nevertheless, the formation of  $(\text{Ti},\text{Mo})_5\text{Si}_3$  precipitates can have a strengthening effect, if they remain comparably small. Thota et al. [13] has demonstrated that during creep at 100 MPa and at 1200 °C strengthening in the AC occurs resulting in a distinct minimum creep rate due to the formation of a high number of  $(\text{Ti},\text{Mo})_5\text{Si}_3$  precipitates with particle sizes of 52 nm ( $d_{50}$ ) to 145 nm ( $d_{90}$ ). These precipitates were found in Ref. [13] to be coherent in certain orientations, even though no particle cutting has been reported or observed yet. However, the creep rate drastically increases as soon as the particle size further increases due to the additional exposure time during creep

at 1200 °C. In case of DED, the particle size of the  $(\text{Ti},\text{Mo})_5\text{Si}_3$  precipitates after manufacturing of 75 nm ( $d_{50}$ ) and 125 nm ( $d_{90}$ ) is comparable to the size of the particles found by Thota et al. [13] for the minimum creep rate.

Therefore, no additional strengthening of the precipitates at higher temperatures is expected in DED in its current processing conditions. However, applying a subsequent heat treatment similar to that used for HT, followed by cooling quickly enough (i.e. at a rate of 100 K/h, as for HT), will increase the Si content in  $(\text{Mo},\text{Ti},\text{Si})_{\text{ss}}$  due to the higher Si solubility at 1600 °C compared to the processing temperatures during DED. Tuning the processing parameter to increase the Si content in  $(\text{Mo},\text{Ti},\text{Si})_{\text{ss}}$  after manufacturing by increasing the laser power (resulting in higher temperature) has to be seen critically, as this will result in a larger temperature gradient and, therefore, can promote the formation of cracking. Reducing the laser powder to prevent the formation of precipitates could also lead to the formation of cracks as the temperature might not surpass the BDTT of approx. 1100 °C. Further investigations would be necessary in order to clarify this issue.

Finally, contribution of diffusion-controlled creep deformation to the onset of plastic deformation due to the high phase boundary density and a homologous temperature of  $T_h$  close to 0.6 at a testing temperature of 900 °C may be conceivable [34]. Even though, the initial strain rate of  $10^{-3} \text{ s}^{-1}$  is much higher compared to the previous results regarding the creep behavior of AC and HT at a much lower test temperature (900 °C vs 1200 °C) [10, 13], a significant contribution by creep to cause the lower  $\sigma_{0.2}$  of the DED condition can still be expected. In contrast to the AC and HT condition, DED shows a higher sensitivity of  $\sigma_{0.2}$  to varying  $\dot{\epsilon}$  (see Fig. 4c). In addition, the creep rate determined by the compression creep experiment for DED and AC confirms that the extrapolation of  $\dot{\epsilon}$  for 200 MPa in Fig. 4c is valid and can be used for the Arrhenius plot in Fig. 4d. Here, the results of AC and HT match well with previous results determined by creep experiments, while the creep rate of DED is two orders of magnitude higher. Therefore, we conclude the finer microstructure of the DED condition provides a high number of fast diffusion paths along the phase boundaries and will enhance diffusional creep. This is also supported by  $\sigma_{0.2}$  of AC becoming smaller compared to HT at temperatures above 900 °C due to its reduced microstructural length scale. Furthermore,



the reduced solid solution strengthening by Si in  $(\text{Mo,Ti,Si})_{\text{ss}}$  is also expected to reduce the creep resistance of the alloy manufactured by DED compared to AC and HT [20]. It is noteworthy, that the apparent stress exponent  $n$  calculated from strain rate sensitivity in Eq. (4) remains small for DED compared to AC and HT at higher strain rates ( $-5$  vs.  $-25$ ), while it is similar at lower strain rates ( $-5$ ). This suggests that the creep mechanism at higher strain rates for AC and HT might be influenced by the interaction of dislocations with precipitates that will form during creep [34], as reported for this alloy at 1200 °C test temperature in Fig. 4a of Ref. [13]. In the case of DED, no such interactions between dislocations and precipitates appear to occur. However, further investigation is required to elucidate the creep mechanism of DED.

## Conclusion

The following conclusions can be drawn from the investigations presented above:

- Mo-20Si-52.8Ti can be successfully manufactured by DED without crack formation and with a porosity of less than 1 vol%. The microstructure of the DED condition is much finer compared to the AC condition due to the higher solidification rate associated with the DED process.
- The mechanical properties of Mo-20Si-52.8Ti are influenced by the microstructural length scale and precipitate formation depending on the processing. At room temperature, the hardness is higher for DED compared to AC and HT, due to the higher phase boundary density. At the same time, the size of the  $(\text{Ti,Mo})_5\text{Si}_3$  precipitates have no significant influence on the RT hardness. At temperatures at and above 900 °C, AC and HT have a higher yield strength  $\sigma_{0.2}$ . The main reasons are (i) creep deformation that contributes in DED to the onset of macroscopic plastic deformation at 900 °C (homologous temperature of approx. 0.6) and (ii) higher number of  $(\text{Ti,Mo})_5\text{Si}_3$  precipitates in  $(\text{Mo,Ti,Si})_{\text{ss}}$  of DED compared to AC and HT reducing the solid solution strengthening by Si.
- The texture of  $(\text{Ti,Mo})_5\text{Si}_3$  in the DED condition and the higher O content of the DED condition compared to AC and DED have no influence on  $\sigma_{0.2}$ .
- High strain rate sensitivity of the DED condition indicates higher contribution by creep deformation compared to AC and HT, which is indeed reflected in the two orders of magnitude lower creep resistance at 900 °C.

## Acknowledgements

We gratefully acknowledge financial support by the Deutsche Forschungsgemeinschaft (DFG) within the framework of HE 1872/38-1 and GRK 2561 MatCom-ComMat. This work was partly carried out with the support of the Karlsruhe Nano Micro Facility (KNMFi, [www.knmf.kit.edu](http://www.knmf.kit.edu)), a Helmholtz Research Infrastructure at Karlsruhe Institute of Technology (KIT, <http://www.kit.edu>). We are also thankful for the financial support extended by the project DST/INT/DFG/P-02-2019.

## Author contributions

Daniel Schliephake: Methodology, Investigation, Formal analysis, Data Curation, Visualization, Project administration, Writing—Original Draft, Writing—Review & Editing. Sri R. Ramdoss: Formal analysis, Writing—Original Draft, Writing—Review & Editing. R.J. Vikram: Formal analysis, Writing—Original Draft, Writing—Review & Editing. Gabriely Falcão: Investigation, Writing—Original Draft, Writing—Review & Editing. Frauke Hinrichs: Investigation, Writing—Review & Editing. Christopher Zenk: Investigation, Writing—Review & Editing. Alexander Kauffmann: Formal analysis, Supervision, Writing—Original Draft, Writing—Review & Editing. Florian Galgon: Methodology, Investigation, Writing—Review & Editing. Satyam Suwas: Supervision, Funding acquisition, Writing—Review & Editing. Ruth Schwaiger: Supervision, Funding acquisition, Writing—Review & Editing. Martin Heilmaier: Supervision, Resources, Funding acquisition, Writing—Review & Editing.

## Funding

Open Access funding enabled and organized by Projekt DEAL.

## Data availability

The data presented in this study are available in KITO-pen at <https://doi.org/10.35097/pgppvxcdzrwjn3ns> under CC BY-SA 4.0 license. Further information is available upon request with [daniel.schliephake@kit.edu](mailto:daniel.schliephake@kit.edu).

## Declarations

**Conflict of interest** The authors declare no conflict of interest.

**Open Access** This article is licensed under a Creative Commons Attribution 4.0 International License, which permits use, sharing, adaptation, distribution and reproduction in any medium or format, as long as you give appropriate credit to the original author(s) and the source, provide a link to the Creative Commons licence, and indicate if changes were made. The images or other third party material in this article are included in the article's Creative Commons licence, unless indicated otherwise in a credit line to the material. If material is not included in the article's Creative Commons licence and your intended use is not permitted by statutory regulation or exceeds the permitted use, you will need to obtain permission directly from the copyright holder. To view a copy of this licence, visit <http://creativecommons.org/licenses/by/4.0/>.

## References

- [1] Pollock TM, Tin S (2006) Nickel-based superalloys for advanced turbine engines: chemistry, microstructure and properties. *J Propul Power* 22:361–374. <https://doi.org/10.2514/1.18239>
- [2] Li MH, Sun XF, Li JG, Zhang ZY, Jin T, Guan HR, Hu ZQ (2003) Oxidation behavior OF a single-crystal Ni-base superalloy in air. I: At 800 and 900°C. *Oxid Met* 59:591–605. <https://doi.org/10.1023/A:1023604214245>
- [3] Zhao S, Xie X, Smith GD, Patel SJ (2003) Microstructural stability and mechanical properties of a new nickel-based superalloy. *Mater Sci Eng A* 355:96–105. [https://doi.org/10.1016/S0921-5093\(03\)00051-0](https://doi.org/10.1016/S0921-5093(03)00051-0)
- [4] Dimiduk DM, Perepezko JH (2003) Mo-Si-B alloys: developing a revolutionary turbine-engine material. *MRS Bull* 28:639–645. <https://doi.org/10.1557/mrs2003.191>
- [5] Perepezko JH, Krüger M, Heilmaier M (2021) Mo-silicide alloys for high-temperature structural applications. *Mater Perform Charact* 10:122–145. <https://doi.org/10.1520/MPC20200183>
- [6] Bewlay BP, Jackson MR, Subramanian PR, Zhao J-C (2003) A review of very-high-temperature Nb-silicide-based composites. *Metall Mat Trans A* 34:2043–2052. <https://doi.org/10.1007/s11661-003-0269-8>
- [7] Lemberg JA, Ritchie RO (2012) Mo-Si-B alloys for ultrahigh-temperature structural applications. *Adv Mater* 24:3445–3480. <https://doi.org/10.1002/adma.201200764>
- [8] Senkov ON, Miracle DB, Chaput KJ, Couzinie J-P (2018) Development and exploration of refractory high entropy alloys – a review. *J Mater Res* 33:3092–3128. <https://doi.org/10.1557/jmr.2018.153>
- [9] Miracle DB, Senkov ON, Frey C, Rao S, Pollock TM (2024) Strength vs temperature for refractory complex concentrated alloys (RCCAs): A critical comparison with refractory BCC elements and dilute alloys. *Acta Mater* 266:119692. <https://doi.org/10.1016/j.actamat.2024.119692>
- [10] Schliephake D, Kauffmann A, Cong X, Gombola C, Azim M, Gorr B, Christ H-J, Heilmaier M (2019) *Intermetallics* 104:133–142. <https://doi.org/10.1016/j.intermet.2018.10.028>
- [11] Obert S, Kauffmann A, Heilmaier M (2020) *Acta Mater* 184:132–142. <https://doi.org/10.1016/j.actamat.2019.11.045>
- [12] Supatatawanich V, Johnson DR, Liu CT (2004) Oxidation behavior of multiphase Mo-Si-B alloys. *Intermetallics* 12:721–725. <https://doi.org/10.1016/j.intermet.2004.02.011>
- [13] Thota H, Schliephake D, Kauffmann A, Wu H, Pundt A, Heilmaier M, Eggeler YM (2024) The creep-induced micro- and nanostructural evolution of a eutectic Mo–Si–Ti alloy at 1200 °C. *Adv Eng Mater*. <https://doi.org/10.1002/adem.202301909>
- [14] Tirunilai AS, Hinrichs F, Schliephake D, Engstler M, Mücklich F, Obert S, Winkens G, Kauffmann A, Heilmaier M (2022) Phase continuity, brittle to ductile transition temperature, and creep behavior of a eutectic Mo–20Si–52.8 Ti alloy. *Adv Eng Mater* 24(11):2200918
- [15] Krüger M, Jain P, Kumar KS, Heilmaier M (2014) Correlation between microstructure and properties of fine grained Mo–Mo3Si–Mo5SiB2 alloys. *Intermetallics* 48:10–18. <https://doi.org/10.1016/j.intermet.2013.10.025>

- [16] Krüger M, Schliephake D, Jain P, Kumar KS, Schumacher G, Heilmaier M (2013) Effects of Zr additions on the microstructure and the mechanical behavior of PM Mo-Si-B alloys. *JOM* 65:301–306. <https://doi.org/10.1007/s11837-012-0475-1>
- [17] Vikram RJ, Schliephake D, Namadi M, Choudhury A, Kauffmann A, Suwas S, Heilmaier M (2025) Strategic alloy design and processing for improved mechanical response in the Mo-Si-Ti system. *Scripta Mater* 255:116341. <https://doi.org/10.1016/j.scriptamat.2024.116341>
- [18] Vikram RJ, Armanda SK, Schliephake D, Kauffmann A, Choudhury A, Heilmaier M, Suwas S (2024) Unveiling the intricacies of a ductile-phase toughened intermetallic: an in-depth exploration of a eutectic Mo-Si-Ti alloy and its mechanical behavior. *Adv Eng Mater*. <https://doi.org/10.1002/adem.202301843>
- [19] Sakidja R, Perepezko JH, Kim S, Sekido N (2008) Phase stability and structural defects in high-temperature Mo-Si-B alloys. *Acta Mater* 56:5223–5244. <https://doi.org/10.1016/j.actamat.2008.07.015>
- [20] Jain P, Kumar KS (2010) Dissolved Si in Mo and its effects on the properties of Mo-Si-B alloys. *Scripta Mater* 62:1–4. <https://doi.org/10.1016/j.scriptamat.2009.09.008>
- [21] Körner C (2016) Additive manufacturing of metallic components by selective electron beam melting — a review. *Inter Mater Rev* 61:361–377. <https://doi.org/10.1080/09506608.2016.1176289>
- [22] Yap CY, Chua CK, Dong ZL, Liu ZH, Zhang DQ, Loh LE, Sing SL (2015) Review of selective laser melting: materials and applications. *Appl Phys Rev* 2:041101. <https://doi.org/10.1063/1.4935926>
- [23] Fichtner D, Schmelzer J, Yang W, Heinze C, Krüger M (2021) Additive manufacturing of a near-eutectic Mo-Si-B alloy: processing and resulting properties. *Intermetallics* 128:107025. <https://doi.org/10.1016/j.intermet.2020.107025>
- [24] Schmelzer J, Rittinghaus S-K, Weisheit A, Stobik M, Paulus J, Gruber K, Wessel E, Heinze C, Krüger M (2019) Printability of gas atomized Mo-Si-B powders by laser metal deposition. *Int J Refract Met Hard Mater* 78:123–126. <https://doi.org/10.1016/j.ijrmhm.2018.08.016>
- [25] Takeda T, Zhou W, Nomura N, Yoshimi K (2022) Mechanical responses of additively manufactured MoSiBTiC alloy under tensile and compressive loadings. *Mater Sci Eng A* 839:142848. <https://doi.org/10.1016/j.msea.2022.142848>
- [26] Higashi M, Yoshimi K (2021) Electron beam surface melting of MoSiBTiC alloys: Effect of preheating on cracking behavior and microstructure evolution. *Mater Des* 209:110010. <https://doi.org/10.1016/j.matdes.2021.110010>
- [27] Vock S, Klöden B, Kirchner A, Weißgräber T, Kieback B (2019) Powders for powder bed fusion: a review. *Prog Addit Manuf* 4:383–397. <https://doi.org/10.1007/s40964-019-00078-6>
- [28] Kirka MM, Lee Y, Greeley DA, Okello A, Goin MJ, Pearce MT, Dehoff RR (2017) Strategy for texture management in metals additive manufacturing. *JOM* 69:523–531. <https://doi.org/10.1007/s11837-017-2264-3>
- [29] Hinrichs F, Kauffmann A, Schliephake D, Seils S, Obert S, Ratschbacher K, Allen M, Pundt A, Heilmaier M (2021) Flexible powder production for additive manufacturing of refractory metal-based alloys. *Metals* 11:1723. <https://doi.org/10.3390/met11111723>
- [30] Schneider CA, Rasband WS, Eliceiri KW (2012) NIH Image to ImageJ: 25 years of image analysis. *Nat methods* 9(7):671–675
- [31] Kurzydowski KJ, Ralph B (1995) The quantitative description of the microstructure of materials. CRC Press
- [32] Nelson JB, Riley DP (1945) An experimental investigation of extrapolation methods in the derivation of accurate unit-cell dimensions of crystals. *Proc Phys Soc London* 57:160. <https://doi.org/10.1088/0959-5309/57/3/302>
- [33] Obert S, Kauffmann A, Seils S, Schellert S, Weber M, Gorr B, Christ H-J, Heilmaier M (2020) On the chemical and microstructural requirements for the pesting-resistance of Mo-Si-Ti alloys. *J Mater Res Technol* 9:8556–8567. <https://doi.org/10.1016/j.jmrt.2020.06.002>
- [34] Kassner ME (2015) Fundamentals of Creep in Metals and Alloys. Butterworth-Heinemann. <https://doi.org/10.1016/C2012-0-06071-1>
- [35] Zhong C, Gasser A, Schopphoven T, Poprawe R (2015) Experimental study of porosity reduction in high deposition-rate laser material deposition. *Opt Laser Technol* 75:87–92. <https://doi.org/10.1016/j.optlastec.2015.06.016>
- [36] España FA, Balla VK, Bandyopadhyay A (2011) Laser processing of bulk Al-12Si alloy: influence of microstructure on thermal properties. *Philos Mag* 91:574–588. <https://doi.org/10.1080/14786435.2010.526650>
- [37] Shao J, Yu G, He X, Li S, Chen R, Zhao Y (2019) Grain size evolution under different cooling rate in laser additive manufacturing of superalloy. *Opt Laser Technol* 119:105662. <https://doi.org/10.1016/j.optlastec.2019.105662>
- [38] Park G-W, Shin S, Kim J-Y, Koo Y-M, Lee W, Lee K-A, Park SS, Jeon JB (2022) Analysis of solidification microstructure and cracking mechanism of a matrix high-speed steel deposited using directed-energy deposition. *J Alloys Compd* 907:164523. <https://doi.org/10.1016/j.jallcom.2022.164523>



- [39] Nedjad SH, Yildiz M, Saboori A (2023) Solidification behaviour of austenitic stainless steels during welding and directed energy deposition. *Sci Technol Weld Joining* 28:1–17. <https://doi.org/10.1080/13621718.2022.2115664>
- [40] Gibson I, Rosen D, Stucker B, Khorasani M (2021) *Additive Manufacturing Technologies*, 3rd edn. Springer Nature Switzerland, Cham
- [41] Raghavan N, Simunovic S, Dehoff R, Plotkowski A, Turner J, Kirka M, Babu S (2017) Localized melt-scan strategy for site specific control of grain size and primary dendrite arm spacing in electron beam additive manufacturing. *Acta Mater* 140:375–387. <https://doi.org/10.1016/j.actamat.2017.08.038>
- [42] Kumar A, Eyre BL (1980) Grain boundary segregation and intergranular fracture in molybdenum. *Proc R Soc Lond A* 370:431–458. <https://doi.org/10.1098/rspa.1980.0043>
- [43] Goldstein JI, Choi SK, Von Loo FJJ, Bastin GF, Metselarr R (1995) Solid-state Reactions and Phase Relations in the Ti-Si-O System at 1373 K. *J Am Ceram Soc* 78:313–322. <https://doi.org/10.1111/j.1151-2916.1995.tb08802.x>
- [44] Northcott L (1956) *Molybdenum (Metallurgy of Rarer Metals)*. Academic Press, New York
- [45] Kishida K, Fujiwara M, Adachi H, Tanaka K, Inui H (2010) Plastic deformation of single crystals of Ti<sub>5</sub>Si<sub>3</sub> with the hexagonal D88 structure. *Acta Mater* 58:846–857. <https://doi.org/10.1016/j.actamat.2009.09.062>
- [46] Jiao Y, Huang LJ, Geng L, Li XT, Gao YN, Qian MF, Zhang R (2017) Nano-scaled Ti<sub>5</sub>Si<sub>3</sub> evolution and strength enhancement of titanium matrix composites with two-scale architecture via heat treatment. *Mater Sci Eng A* 701:359–369. <https://doi.org/10.1016/j.msea.2017.06.067>
- [47] Massalski TB, Okamoto H, Subramanian PR, Kacprzak L (1990) *Binary Alloy Phase Diagrams*, 2nd edn. ASM International, Materials Park
- [48] Krüger M, Franz S, Saage H, Heilmaier M, Schneibel JH, Jéhanno P, Böning M, Kestler H (2008) Mechanically alloyed Mo–Si–B alloys with a continuous  $\alpha$ -Mo matrix and improved mechanical properties. *Intermetallics* 16:933–941. <https://doi.org/10.1016/j.intermet.2008.04.015>
- [49] Winkens G, Kauffmann A, Herrmann J, Czerny AK, Obert S, Seils S, Boll T, Baruffi C, Rao Y, Curtin WA, Schwaiger R, Heilmaier M (2023) The influence of lattice misfit on screw and edge dislocation-controlled solid solution strengthening in Mo-Ti alloys. *Commun Mater*. <https://doi.org/10.1038/s43246-023-00353-8>
- [50] Sturm D, Heilmaier M, Schneibel JH, Jéhanno P, Skrotzki B, Saage H (2007) The influence of silicon on the strength and fracture toughness of molybdenum. *Mater Sci Eng A* 463:107–114. <https://doi.org/10.1016/j.msea.2006.07.153>

**Publisher's Note** Springer Nature remains neutral with regard to jurisdictional claims in published maps and institutional affiliations.